Original Paper

Methane Adsorption Characteristics Under In Situ Reservoir Conditions of the Wufeng–Longmaxi Shale in Southern Sichuan Basin, China: Implications for Gas Content Evaluation

Chao Qian,[1,2,3] **Xizhe Li,**[2,6] **Qing Zhang,**[1] **Yanchao Li,**[1] **Weijun Shen** ,[3,4,6] **Hongchuan Xing,**[1] **Pinghua Shu,**[1] **Lingling Han,**[2,5] **Yue Cui,**[2,5] **and Yize Huang**[2,5]

The accuracy of adsorbed gas content under actual in situ reservoir conditions is crucial for the evaluation of shale gas reserves. In this study, the characteristics of methane adsorption on the Wufeng–Longmaxi shale were investigated under a wide range of pressure (0–51 MPa) and actual in situ water saturation. Methane–shale adsorption exhibits the Gibbs excess adsorption phenomenon at high pressure. The excess adsorption amount needs be corrected to absolute adsorption amount, otherwise it will be seriously underestimated. The optimal supercritical methane adsorption model was determined by the corrected Akaike's Information Criterion method. The methane adsorption amount of shale samples ranged from 1.521 to 4.079 m^3/t. Adsorption capacity was dominated by the total organic carbon content as well as micropore volume and total specific surface area. Additionally, pore volume and specific surface area were contributed mainly by abundant micropores associated with organic matter. Thermodynamic parameters revealed that the adsorption of methane on shale was an exothermic process. As the temperature increased from 40 to 80 °C, the methane adsorption capacity decreased from 4.27 to 2.99 m^3/t, a 30% decrease. The actual in situ water saturation correlated primarily with clay content, regardless of clay types, and increased with clay content. The formation of an adsorbed water film and the blockage of pores for gas adsorption by clusters of water molecules significantly lowered the adsorption capacity. The relative difference in the adsorption capacity increased with water saturation, with the adsorption capacity of water-bearing shales decreasing by 21–84% at a water saturation of 30–71% compared to dry shales.

KEY WORDS: Wufeng–Longmaxi shale, In situ reservoir condition, Thermodynamic parameters, Water saturation, Adsorption capacity.

[1]Shale Gas Exploration and Development Department, CNPC Chuanqing Drilling Engineering Co., Ltd., Chengdu 610051, Sichuan, China.

[2]Research Institute of Petroleum Exploration and Development, Beijing 100083, China.

[3]Key Laboratory for Mechanics in Fluid Solid Coupling Systems, Institute of Mechanics, Chinese Academy of Sciences, Beijing 100190, China.

[4]School of Engineering Science, University of Chinese Academy of Sciences, Beijing 100049, China.

[5]Institute of Porous Flow and Fluid Mechanics, Chinese Academy of Sciences, Langfang 065007, China.

[6]To whom correspondence should be addressed; e-mail: lxz_cnpc@outlook.com, lxz69@petrochina.com.cn, wjshen763@imech.ac.cn

INTRODUCTION

The 'shale revolution' triggered by long horizontal drilling coupled with multi-stage hydraulic fracturing techniques has addressed the energy gap in USA (Hughes, 2013; Middleton et al., 2017). China's shale gas resources are estimated to be 144.5×10^{12} m³, with recoverable resources of 36×10^{12} m³ (Zou et al., 2010; Jia et al., 2012; Ma et al., 2020; Nie et al., 2022). The majority of the shale gas is either adsorbed gas or free gas, with a little amount dissolved in reservoir fluid (Curtis, 2002; Hao et al., 2013; Middleton et al., 2017). Adsorbed gas accounts for 20–85% and 27.1–47.8% of the total in the shale gas reservoirs in North America and in Wufeng–Longmaxi in the Sichuan Basin, respectively (Curtis, 2002; Hao et al., 2013; Borjigin et al., 2017). For the appraisal of shale gas reserves, the accuracy of adsorbed gas content at actual in situ reservoir condition is crucial (Stueck et al., 2016).

A common and valid method for determining the content of adsorbed gas is the methane–shale adsorption test similar to that for coalbed methane (Rexer et al., 2014; Wang et al., 2016; Zhou et al., 2018). However, the conditions of previous tests were far lower than the actual in situ reservoir temperature (80–120 °C) and pressure (> 30 MPa) of the Wufeng–Longmaxi Formation in the Sichuan Basin, suggesting that these results may not be consistent with the actual adsorbed gas content (Chen et al., 2018). The adsorption amount measured by laboratory isothermal adsorption is the excess adsorption amount and follows Gibbs's excess adsorption behavior (Gibbs, 1878; Sakurovs et al., 2007; Rexer et al., 2013; Zhou et al., 2018; Shen et al., 2021). Modeling studies of subcritical gas adsorption isotherms based on the theories of Langmuir monolayer adsorption, Brunauer–Emmett–Teller (BET) multilayer adsorption, Dubinin–Astakhov (DA), and Dubinin–Radushkevich (DR) pore volume filling of micropore have been carried out (Langmuir, 1918; Brunauer et al., 1938; Dubinin & Astakhov, 1971; Sakurovs et al., 2007; Dang et al., 2020). However, the supercritical excess adsorption isotherms cannot be characterized directly by subcritical gas adsorption due to the nature of supercritical gases (Zhou et al., 2018; Dang et al., 2020).

The primary determinants of methane–shale adsorption capacity are the composition of the shale (organic matter and minerals), pore structure, water saturation, and reservoir temperature and pressure characteristics (Ji et al., 2012; Hao et al., 2013; Wang et al., 2021; Xu et al., 2021). Approximately 16.3–46.7% of the adsorption capacity can be attributed to clay minerals due to their larger negatively charged specific surface area (SSA) (Yang et al., 2015; Zhu et al., 2020). The water saturation in in situ shale reservoirs typically ranges from 10 to 35% in North American shale gas reservoirs and from 10 to 90% in the Sichuan Basin (Chalmers & Bustin, 2008; Gasparik et al., 2014; Zou et al., 2019). The adsorption capacity of Devonian–Mississippian and Jurassic shales in the northeastern British Columbia basin, Canada, at equilibrium moisture is 58.3% and 71.5% of that in the dry state, respectively (Hao et al., 2013). The amount of adsorbed gas would be overestimated if the water content of the reservoirs is overlooked. However, the previous studies usually determined at the full moisture-equilibrated shale. Thus, the methane adsorption test on water-bearing shale at the in situ water saturation is required to obtain a more precise estimate of the adsorbed gas content (Yang et al., 2020).

In this study, the characteristics of methane adsorption on Wufeng–Longmaxi shale were investigated under a wide range of pressure (0–51 MPa) and actual in situ water saturation. Supercritical methane excess adsorption models were evaluated using the corrected Akaike's Information Criterion (AICc) method. The effects of shale composition, pore structure, and water saturation on the adsorption capacity were explored thoroughly, and the mechanism of gas adsorption in dry and water-bearing shale was elaborated in detail.

GEOLOGICAL SETTING

The Sichuan Basin is an enormous diamond-shaped basin where marine cratons and continental foreland basins are superimposed on the Upper Yangtze Craton (Xinhua et al., 2019). The present-day tectonic landscape was formed by extensively tectonic movements, surrounded by several orogenic belts, with total area of around 1.8×10^5 km² and total natural gas resources of approximately 39.94×10^{12} m³ (Gou et al., 2021; Li et al., 2021a, 2021b). The Sichuan Basin has been divided into four hydrocarbon accumulation areas based on the nature of the basement, sedimentary characteristics, and hydrocarbon genesis, with the study area located at the southern gas district (Fig. 1a) (Li et al., 2022).

The Wufeng–Longmaxi shale has advantages in terms of shale gas content and hydraulic fracturing due to its abundant organic matter (OM) and siliceous minerals (Guo et al., 2020; Qiu et al., 2020; Han et al., 2022). Prior to Permian, marine sedimentary environment was predominant in the Sichuan Basin, where shale and carbonate rocks were formed. The Wufeng–Longmaxi shale, deposited in deep water, is characterized by its extensive distribution, significant thickness, and abundant OM (Fig. 1b) (Gou et al., 2020).

SAMPLES AND METHODS

Samples

Seven core samples were collected from the depth interval 2716.0–2750.0 m of the Wufeng–Longmaxi Formation shale in Well WY8 in the Weiyuan area (Fig. 1). Sample porosity was measured by the fluid saturation method, and shale bulk density was collected from field test data (Table 1).

TOC and Mineral Composition

The total organic carbon (TOC) content was determined by a carbon/sulfur analyzer based on the reference material GB/T 19145-2003. Prior to the analysis, the core samples were powdered into particles of less than 100 mesh in size. Then, the TOC and inorganic carbon contents were determined by the carbon/sulfur analyzer, and the TOC content is the TOC minus the inorganic carbon content.

The mineral compositions of the shale were determined using the X-ray diffractometer RINT-TTR3 following the Chinese oil and gas industry standard (SY/T) 5163-2018. Then, the area under the curve of the major peak per mineral was used to estimate the mineral composition semi-quantitatively (Ross & Bustin, 2008).

Low Pressure CO_2 and N_2 Gas Adsorption

The BeiShiDe PS2 fully automated specific surface area analyzer was used to carry out low pressure gas adsorption experiments based on the reference material GB/T 10722-2014. The core samples were powdered into particles of 60–80 mesh (180–250 μm) and dried at 110 °C for 24 h before the gas adsorption tests. N_2 adsorption tests were carried out at 77.35 K with relative pressure (P/P_0) of 0.04–0.98 (Zhang et al., 2020a, 2020b). The CO_2 adsorption experiments were carried out at 273 K with relative pressure (P/P_0) of 0.001–0.03.

The non-local density functional theory (NLDFT) method, more advanced in characterizing micropores and mesopores, was selected to interpret the pore structure (Wei et al., 2016). Combination of CO_2 and N_2 adsorption isotherms data can characterize the full-scale nanopores of shale, with an effective detection size of 0.3–1.5 nm for CO_2 and 1.5–100 nm for N_2 (Gou et al., 2021).

Field Emission–Scanning Electron Microscopy (FE–SEM) Observation

Prior to the experiment, the surfaces of the shale samples were first finely ground, and argon ion polished via Leica EM RES 102 ion milling polisher. Gold was then sprayed onto the polished surface to improve conductivity and provide clear views and images (Qian et al., 2022). FE–SEM observations were made by using the Crosbeam540 scanning electron microscope. FE–SEM images help to understand the type, distribution, morphology, and size of micro-nanopores (Loucks et al., 2009; Yang et al., 2016a, 2016b; Zhang et al., 2020a, 2020b).

Water Uptake and Water Saturation Restoration

Due to long-term exposure to the air, the original moisture of shale cores extracted from the ground will be lost. Thus, the key to the methane adsorption experiment under the in situ shale reservoir water saturation condition is to restore the water saturation of the dry samples based on the water saturation determined at the coring site. The water uptake and water saturation restoration experiments were as follows:

(1) The experimental apparatus was the BeiShiDe Vacuum Vapor/Gas Sorption Analyzer. An elaborated explanation of the workflow and function of the experimental apparatus can be found in Dang et al. (2020). The dry shale powders in 60–80 mesh (approximately 1 g) were placed at the workstation and degassed. Then, shale water uptake was carried out at 50 °C using the dynamic weight method to
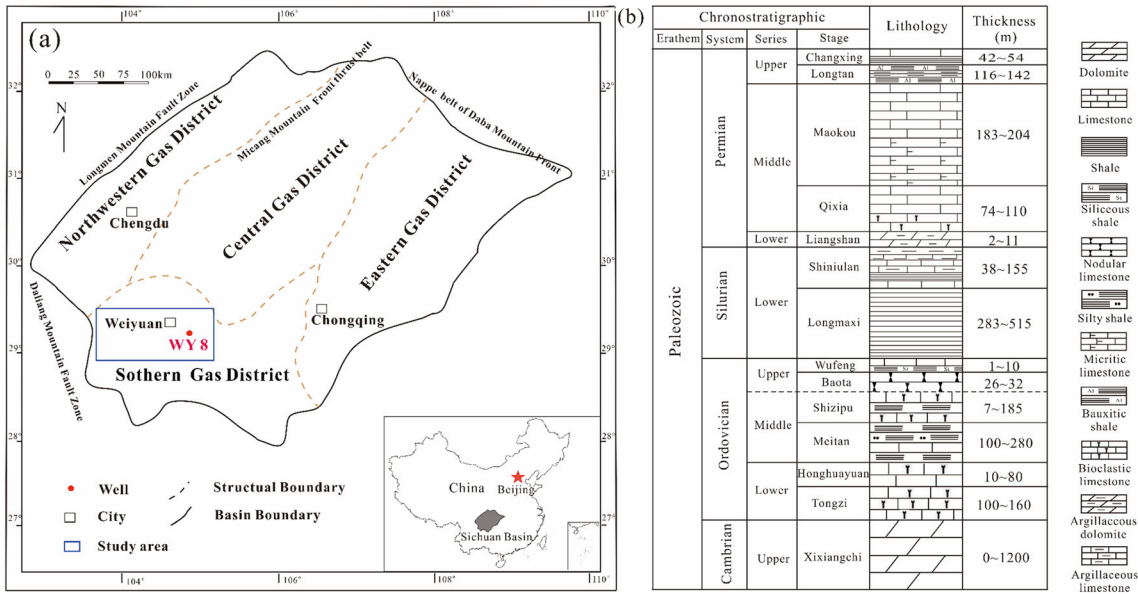
Figure 1. (**a**) Location of study area. (**b**) Stratigraphic units in the study area in southern Sichuan Basin.

Table 1. TOC, porosity, and mineral composition of the Wufeng–Longmaxi shale samples

| Sample ID	Depth (m)	TOC (%)	Porosity (%)	Bulk density (g/cm³)	Mineral composition (%)						Relative content of clay minerals (%)		
					Quartz	Feldspar	Calcite	Dolomite	Pyrite	Total clay	I/S	Illite	Chlorite
WY8-1	2716.90	0.46	4.47	2.61	21.9	3.2	9.1	6.9	7.5	51.4	40	54	6
WY8-2	2720.10	2.53	5.96	2.68	25.3	4.2	22	17.7	3.6	27.2	39	45	16
WY8-4	2744.95	4.70	6.61	2.64	31.8	3.0	15.6	19.6	8.4	21.6	46	44	10
WY8-5	2743.45	2.55	5.77	2.68	43.9	7.7	4.7	5.0	3.1	35.6	42	49	9
WY8-6	2737.52	3.54	5.86	2.65	52.1	5.5	2.9	4.4	4.5	30.6	40	51	9
WY8-7	2734.98	4.20	6.55	2.66	35.4	5.4	10.8	13.5	4.7	30.2	46	46	8
WY8-8	2747.60	3.76	5.84	2.71	66.2	1.9	10.3	8.8	1.5	11.3	20	59	21

obtain the amount of water uptake at different relative humidities. In this work, eight steps of relative humidity (RH) were measured to establish isotherms and the adsorption equilibrium conditions for isothermal adsorption were set at 0.1 mg/60 min (0.01%/60 min). When sample adsorption/desorption equilibrium was reached, the next RH step was automatically entered.

(2) The actual in situ reservoir water content of the shale samples was determined by the water saturation and porosity of the sample measured at the coring site (Tables 1 and 2). This was then matched to the amount of water up-

take to obtain the approximate RH required to restore the actual in situ water saturation. Then, the saturated salt solution with corresponding RH was selected to restore the actual in situ reservoir water content of a dried sample (about 120 g) in a closed thermostatic container (50 °C) (Table 2). The experiment schematic is demonstrated in Figure 2. The reason for restoring the sample water content via saturated salt solutions with corresponding RH is that the binding of water to the shale samples is long-term and stable compared to the dynamic weight method, which facilitates the methane–shale adsorption experiments on

Table 2. Water saturation (S_W), original water content, relative humidity (RH), and saturated salt solution type of shale samples

Sample ID	S_W (in situ) (%)	Original water content (mg/g)	Matched water uptake (mg/g)	RH (%)	Saturated salt solution (50 °C)	S_W (Experimental) (%)
WY8-1	65.67	11.25	12.25	70	NaCl	71.53
WY8-2	53.62	11.92	12.22	70	NaCl	54.95
WY8-4	40.60	10.17	11.07	50	NaBr	44.21
WY8-5	59.95	12.91	13.57	70	NaCl	63.03
WY8-6	39.12	8.65	10.81	50	NaBr	48.88
WY8-7	49.98	12.31	13.42	70	NaCl	54.50
WY8-8	27.78	5.99	6.30	50	NaBr	29.23
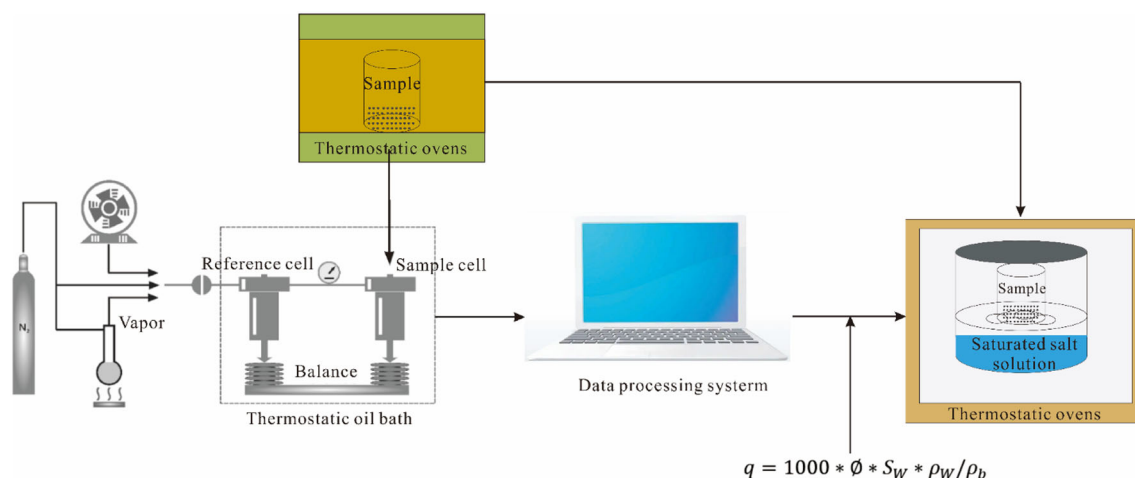
$$q = 1000 * \emptyset * S_W * \rho_W / \rho_b$$

Figure 2. Schematic of experiments for water uptake and actual in situ water content restoring in shale samples.

samples with water saturated restored. The actual in situ water content can be determined as follows:

$$q = 1000 * \varphi * S_W * \rho_W / \rho_b \quad (1)$$

where q is water content (mg/g) φ is porosity (%), which is listed in Table 1, S_W is water saturation (%), which is listed in Table 2, ρ_W is water density (regarded as 1 g/cm^3), and ρ_b is the bulk density of shale (g/cm^3), which is listed in Table 1.

Adsorption of Methane–Shale Under High-Pressure Conditions

The methane–shale adsorption isotherm data were measured via BSD 3H-2000PH adsorption equipment based on the reference material GB/T 35210.2-2020. A detailed explanation of the workflow and function of the experimental apparatus can be found in Shen et al. (2021). Approximately 120 g of shale samples (60–80 mesh) were placed in a sample cell per measurement. The pressure of methane–shale adsorption ranged from 0 to 51 MPa to match the actual in situ reservoir pressure as closely as possible. In addition, sample WY8-6 was selected for methane–shale adsorption experiments at 313.15 K, 333.15 K, and 353.15 K to investigate the impact of temperature. Compared to dry shale, adsorption capacity in water-bearing shale decreases significantly (Wang & Yu, 2016). Water-bearing shale samples were selected for shale–methane adsorption at 333.15 K to obtain the methane adsorption data under the actual in situ shale reservoir water saturation condition. It is crucial to note that degassing was not performed prior to the experiment.

Modeling Study of Supercritical Excess Adsorption

Modeling studies of subcritical gas adsorption isotherms based on the theories of Langmuir monolayer adsorption, BET multilayer adsorption, and DA pore volume filling of micropore were carried out (Langmuir, 1918; Brunauer et al., 1938; Dubinin & Astakhov, 1971). Nevertheless, supercritical methane–shale adsorption is characterized by reduced excess adsorption amount at high pressure. The above adsorption isotherm models are no longer directly applicable, and a correction term needs to be added according to the Gibbs' excess adsorption theory (Dang et al., 2020). In this work, the commonly used Langmuir, BET, and DA subcritical gas adsorption models were selected and an excess adsorption correction term was added to determine the optimal supercritical excess adsorption model based on measured methane–shale adsorption data.

Langmuir-Based Supercritical Methane Excess Adsorption Model: Monolayer Adsorption Theory

The Langmuir model assumptions are as follows: The surface of a solid is energetically homogeneous. The methane molecules are adsorbed in a monolayer; each adsorbed particle occupies only one adsorption site; interactions between the adsorbed molecules are negligible; and the rates of adsorption and desorption have achieved a dynamic equilibrium under certain conditions (Langmuir, 1918; Dang et al., 2020). The model is generally described as follows:

$$n_{\text{abs}} = \frac{V_L P}{P + P_L} \tag{2}$$

where n_{abs} is absolute adsorption amount (m^3/t), V_L is the Langmuir volume (m^3/t), P is the equilibrium adsorption equilibrium pressure (MPa), and P_L is the Langmuir pressure (MPa), i.e., the corresponding pressure when the adsorption amount reaches half of V_L.

The Langmuir model's adsorption isotherm exhibits I-type isotherm adsorption behavior, which is in conflict with the phenomenon that the amount of adsorbed gas decreases under supercritical conditions (Chen et al., 2018; Zhou et al., 2018; Dang et al., 2020). Supercritical shale methane adsorption follows the Gibbs excess adsorption behavior, and

so, the excess adsorption correction term is introduced, and the Langmuir-based supercritical excess adsorption model (S–L) is described as follows:

$$n_{\text{ex}} = \frac{V_L P}{P + P_L}\left(1 - \frac{\rho_{\text{gas}}}{\rho_{\text{ads}}}\right) \tag{3}$$

where n_{ex} is the excess adsorption amount (m^3/t), ρ_{ads} is methane density (g/cm^3) of adsorbed phase, and ρ_{gas} is methane density (g/cm^3) of free phase.

BET-Based Supercritical Methane Excess Adsorption Model: Multilayer Adsorption Theory

The well-known BET model assumes that the surface properties of an adsorbent are homogeneous, gas molecules are adsorbed on solid surfaces in multiple layers, and the interactions and lateral interaction between adsorbed molecules are negligible (Brunauer et al., 1938), as described by:

$$n_{\text{abs}} = \frac{V_{\text{BET}} C P}{(P_0 - P)[1 + (C - 1)(P/P_0)]} \tag{4}$$

where V_{BET} is the maximum monolayer adsorption volume (m^3/t) of the BET model, C is a constant (dimensionless), and P_0 is the saturation vapor pressure (MPa).

Similarly, the introduction of an excess adsorption correction term gives the following BET-based supercritical (S–BET) excess adsorption model:

$$n_{\text{ex}} = \frac{V_{\text{BET}} C P}{(P_0 - P)[1 + (C - 1)(P/P_0)]} \cdot \left(1 - \frac{\rho_{\text{gas}}}{\rho_{\text{ads}}}\right) \tag{5}$$

Equation (5) can be simplified and rearranged as follows (Dang et al., 2020):

$$n_{\text{ex}} = \frac{P}{k_1 + k_2 P + k_3 P^2} \cdot \left(1 - \frac{\rho_{\text{gas}}}{\rho_{\text{ads}}}\right) \tag{6}$$

where k_1, k_2, and k_3 are three fitted parameters defined, respectively, as $k_1 = P_0/V_{\text{BET}} C$, $k_2 = (C - 2)/V_{\text{BET}} C$, and $k_3 = (1 - C)/V_{\text{BET}} C P_0$. However, the saturation vapor pressure cannot be determined accurately under supercritical phase and, when the gas density is used in place of the gas pressure, Eq. (6) becomes:

$$n_{\text{ex}} = \frac{\rho_{\text{gas}}}{k_1 + k_2 \rho_{\text{gas}} + k_3 \rho_{\text{gas}}^2} \cdot \left(1 - \frac{\rho_{\text{gas}}}{\rho_{\text{ads}}}\right) \tag{7}$$

DA-Based Supercritical Methane Excess Adsorption Model: Micropore Filling Theory

Strongly heterogeneous shale has a complex pore structure and a wide range of pore size distributions (Loucks et al., 2009; Borjigin et al., 2017). The DA model is derived from the Polanyi theory, which assumes that methane molecules are sequentially filled into micropores according to the size of the pore adsorption potential (Wang et al., 2016). This DA model can more accurately characterize the behavior of gas adsorption on heterogeneous shale due to consideration of surface heterogeneity (Dubinin & Astakhov, 1971; Dang et al., 2020). The DA model based on the theory of micropore volume filling is described as follows:

$$n_{abs} = V_M \exp\left\{-D\left[\ln\left(\frac{P_0}{P}\right)\right]^n\right\} \qquad (8)$$

where V_M is the maximum adsorption volume (m^3/t) of micropore filling of the DA model, D is pore structure parameter, and n is a constant.

As noted above, the saturation vapor pressure cannot be determined accurately under the supercritical phase and the gas pressure P_0 and P are replaced with the methane density of adsorbed phase ρ_{ads} and free phase ρ_{gas}, respectively. However, we took the Gibbs excess adsorption behavior into account and established the supercritical Dubinin–Astakhov (S–DA) excess adsorption model as follows:

$$n_{ex} = V_M \exp\left\{-D\left[\ln\left(\frac{\rho_{ads}}{\rho_{gas}}\right)\right]^n\right\} \cdot \left(1 - \frac{\rho_{gas}}{\rho_{ads}}\right) \quad (9)$$

In this study, the ρ_{gas} at a given temperature and equilibrium pressure was available at the NIST (https://webbook.nist.gov/chemistry/fluid/) (Dang et al., 2020), and the applicable temperature and pressure ranges were 90.6941–625.0 K and 0–1000 MPa, respectively. In addition, regarding the ρ_{ads} as an undetermined parameter, the value obtained by mathematically optimizing a supercritical methane excess adsorption model combined with experimental data was consistent with the thermodynamic properties of methane and minimizes the discrepancies from experimental data (Zhou et al., 2018).

Thermodynamic Parameters

Thermodynamic parameters provide important information about the adsorption process. Isosteric heat at a specific surface coverage (q_{st}) is the instantaneous enthalpy change (ΔH) of the adsorption process, which reflects the interaction strength between the adsorbate and the adsorbent, and is derived from the Clausius–Clapeyron equation (Dang et al., 2020), thus:

$$\frac{1}{P}\frac{dP}{dT} = \frac{q_{st}}{RT^2} \qquad (10)$$

Deforming and integrating both ends of Eq. (10), it becomes:

$$\ln\frac{P}{P_0} = \frac{-q_{st}}{RT} + \frac{\Delta S}{R} \qquad (11)$$

where P and T are pressure (MPa) and temperature (K) associated with a certain absolute adsorption quantity, P_0 is atmospheric pressure (0.1 MPa), and ΔS is entropy change (J/mol ·K).

Isosteric heat (q_{st}) is equal to ΔH but with a negative sign, thus:

$$q_{st} = -\Delta H \qquad (12)$$

Substituting Eqs. (12) in (11) and deforming it, it becomes:

$$\ln P = \frac{\Delta H}{RT} + \frac{\Delta S}{R} + \ln P_0 \qquad (13)$$

By plotting lnP vs. $1/T$, the ΔH and ΔS can be obtained from the slope and intercept, respectively, of the fitting line. The standard Gibbs free energy change (ΔG) can be used to determine the direction and limit of the spontaneous thermodynamic process of adsorbate adsorption on adsorbents under isothermal and isobaric conditions, and it can be obtained as follows:

$$\Delta G = \Delta H - T\Delta S \qquad (14)$$

RESULTS

Geochemical Characteristics

The TOC content, porosity, shale bulk density, and mineral composition are listed in Table 1. Quartz, carbonate, and clay minerals predominate in shale, ranged from 21.9 to 66.2% (average 39.5%),
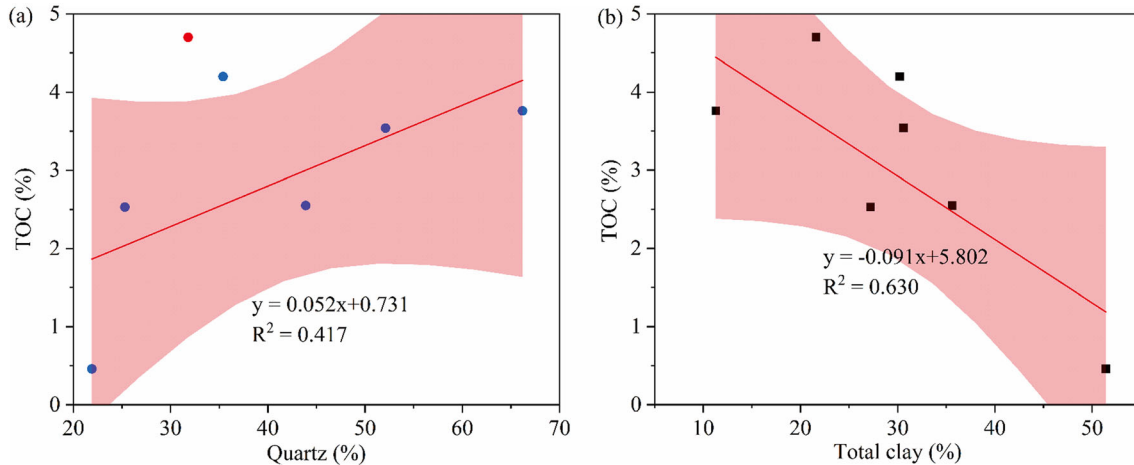
Figure 3. Relationship between TOC content and mineral composition.

7.3 to 39.7% (average 21.6%), and 11.3 to 51.4% (average 29.7%), respectively. The TOC contents were 0.46–4.70% (average 3.11%), indicating that it is favorable for shale gas reserves and production (Fan et al., 2020; Ma et al., 2020). The TOC content is weakly correlated with quartz content ($R^2 = 0.417$) (Fig. 3a). The reason for this is that the Wufeng–Longmaxi shale is rich in bio-fossils (graptolites, radiolarians and spicules, etc.) deposited in a deep-water shelf environment and its siliceous minerals are mainly biogenic, whereas the anoxic deep-water shelf environment facilitated OM enrichment and preservation (Guo et al., 2020). However, clay minerals are usually mainly derived from terrigenous clastic material, with lower TOC and siliceous contents (Guo et al., 2020), and so, the TOC content has a negative relationship with the content (Fig. 3b).

Characteristics of Pore Structure

Pore Characteristics from FE–SEM Observation

The equivalent reflectance of vitrinite (EqRo) of the Wufeng–Longmaxi shales is greater than 2%, and the OM is in the overmature gas generation stage (Qian et al., 2022). OM in the overmature Wufeng–Longmaxi shale is dominated by pyrobitumen and graptolites accounting for over 90% of the total. Pyrobitumen is found primarily as matrix bitumen in matrices and occurs in mixtures with flaky clay and fillings of fossil cavities (Teng et al., 2022). Organic pores are found mainly in the interior or edge of pyrobitumen based on FE–SEM observation. The pore shapes are oval, bubble-shaped, or sponge-shaped in the transection section, and ink-bottle shaped in the three-dimensional space with pore widths ranging from a few to several hundred nanometers, which have good connectivity (Fig. 4a and b) (Loucks et al., 2009; Yang et al., 2016a, 2016b; Peng, 2019; Zhang et al., 2020a, 2020b).

Interparticle (InterP) and intraparticle (IntraP) pores are the most common types of inorganic pores (Loucks et al., 2009). InterP pores are usually found between clay and brittle minerals (such as quartz, calcite, and dolomite) grains, with triangular, polygonal or slit-shaped shapes. Intrap pores within clays are formed by the transformation of minerals during burial and diagenesis (Loucks et al., 2012), with pore widths varying between tens of nanometers and several microns and irregular, triangular, and elliptical shapes (Fig. 4c). Strawberry pyrite is commonly found in the Wufeng–Longmaxi shale samples, and the InterP pores associated with strawberry pyrite are formed by non-compact aggregation of pyrite crystals during growth (Fig. 4d).

Pore Characteristics from Gas Adsorption

According to the IUPAC classification scheme, pores are classified as micropore (< 2 nm), meso-
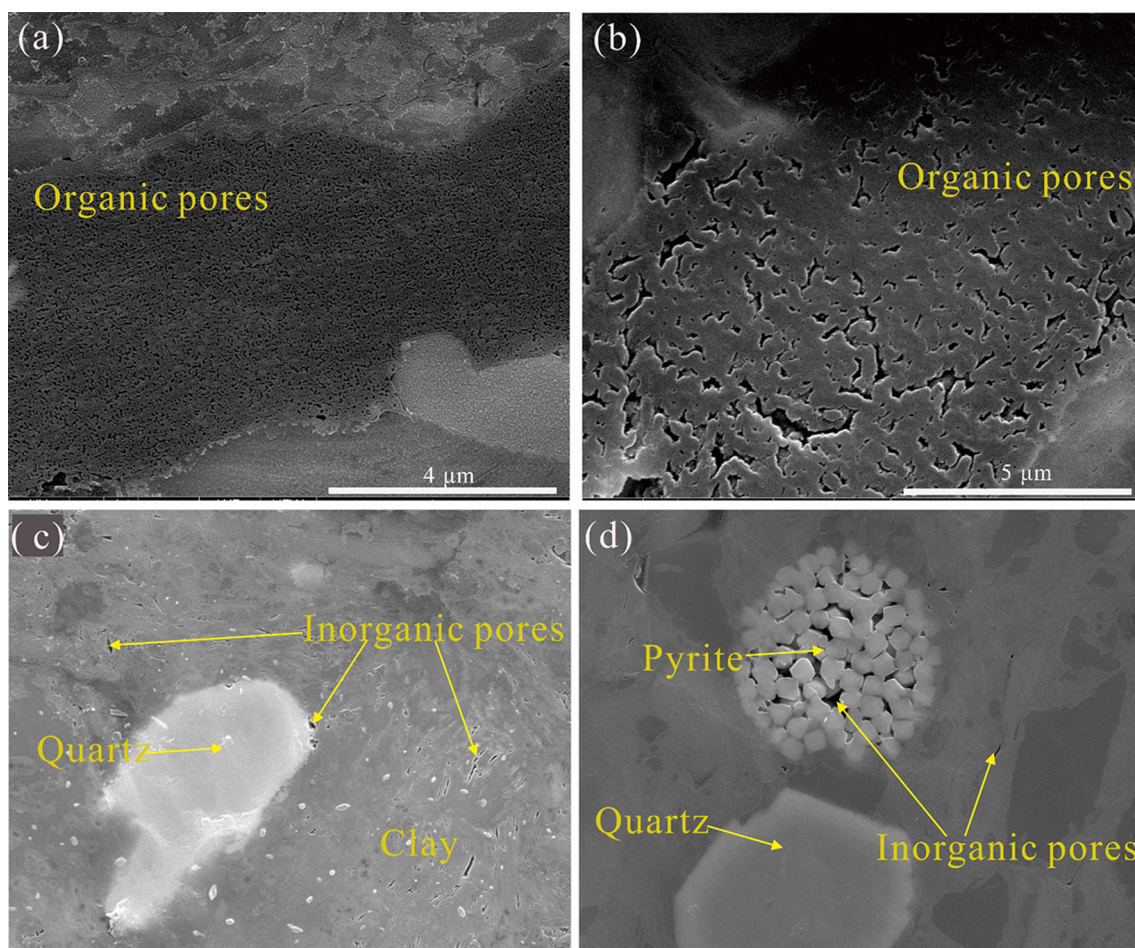
Figure 4. FE–SEM images of the shale samples: (**a**), (**b**) organic pores; (**c**), (**d**) inorganic pores.

pore (2–50 nm), and macropore (> 50 nm) based on pore size. The CO_2 adsorption isotherms exhibited typical I-type curves according to the IUPAC classification (Fig. 5a) (Sing, 1985), indicating that there was an abundance of micropores in the Wufeng–Longmaxi shale (Xu et al., 2020; Zhang et al., 2020a, 2020b). The micropore size distributions, interpreted based on the NLDFT model, had several peaks in the 0.3–0.9 nm range, revealing that pore volume was contributed mainly by those pores (Fig. 5b). The cumulative micropore volume calculated by CO_2 adsorption isotherms varied between 0.0034 and 0.0077 cm^3/g (Fig. 5c, Table 3).

The N_2 adsorption and desorption isotherms overlap at relative pressures less than 0.45 because the gas was adsorbed in a single molecular layer (Guan et al., 2016). However, a hysteresis loop formed by the adsorption of the N_2 multilayer with relative pressures greater than 0.45 suggests that the pores of the shale were heterogeneous (Fig. 5d) (Zhang et al., 2020a, 2020b). All N_2 adsorption isotherms displayed typical type IV characteristics reported by the IUPAC, suggesting that the Wufeng–Longmaxi shale possesses an open, continuous nanoscale pore system (Sing, 1985; Yang et al., 2014). Furthermore, the shape of the hysteresis loops was similar to a mixture of H2 and H3 types curves reported by the IUPAC, revealing that the pores in the Wufeng–Longmaxi shale were ink-bottle and slit-shaped (Sing, 1985; Zhang et al., 2018; Qian et al., 2022). Ink-bottle pores occur mainly in OM and slit-shaped pores are found usually in clays (Zhang et al., 2020a, 2020b). These results agree with the pore characteristics in FE–SEM images (Fig. 4).

The pore size distributions calculated by the NLDFT model showed a broad peak in the range of
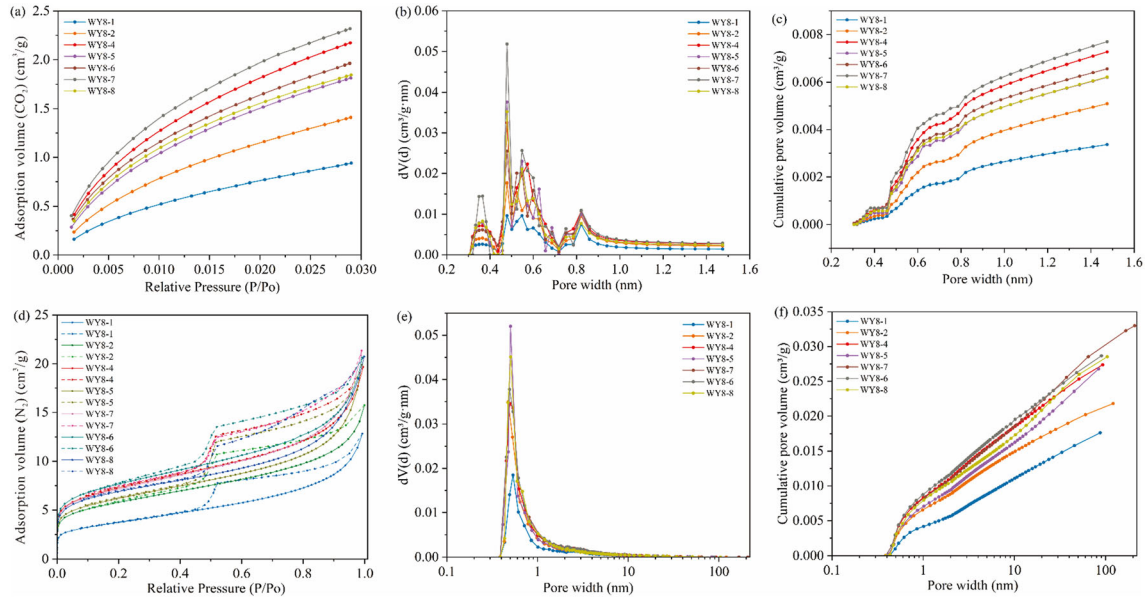
Figure 5. Pore size distributions based on CO_2 and N_2 adsorption isotherms.

Table 3. Pore structure parameters of the Wufeng–Longmaxi Shale samples, southern Sichuan

Sample ID	Pore volume (cm³/g)				Surface area (m²/g)			
	Micropore	Mesopores	Macropores	Total	Micropore	Mesopores	Macropores	Total
WY8-1	0.0034	0.0145	0.0039	0.0218	10.143	2.715	0.267	13.125
WY8-2	0.0051	0.0171	0.0028	0.0250	15.176	5.102	0.150	20.428
WY8-4	0.0073	0.0212	0.0044	0.0329	22.930	2.490	0.271	25.691
WY8-5	0.0062	0.0201	0.0053	0.0316	19.217	2.206	0.498	21.921
WY8-6	0.0066	0.0202	0.0045	0.0313	20.792	4.365	0.262	25.419
WY8-7	0.0077	0.0216	0.0055	0.0348	24.540	2.189	0.350	27.079
WY8-8	0.0062	0.0215	0.0046	0.0324	19.578	4.837	0.288	24.703

0.5–50 nm, demonstrating that pore volume was dominated by those pores (Fig. 5e). The cumulative non-micropore volume calculated by the N_2 adsorption isotherms ranged from 0.0176 to 0.0330 cm³/g, and sample WY8-7 was the largest at 0.0330 cm³/g (Fig. 5f, Table 3).

The total pore volume of all samples ranged from 0.0218 to 0.0348 cm³/g, with mesopores contributing more than 60%; followed by micropores accounting for about 20%. The total SSA varied between 13.125 and 27.079 m²/g and was dominated by micropores, which accounted for more than 75% of the total, followed by mesopores, which accounted for about 16% (Fig. 6, Table 3).

Characteristics of Water Vapor Adsorption and Water Saturation

All the water vapor adsorption isotherms belong to type II curve behavior based on the IUPAC classification (Fig. 7) (Sing, 1985). Three zones can be recognized between the water vapor adsorption isotherms, including a low RH area (RH < 20%), a middle RH area (20% < RH < 85%), and a high RH area (RH > 85%). In the low RH area, the water uptake amount increased rapidly, and water molecules were adsorbed directly in the hydrophilic clay-associated pore spaces of the shale surface as a monolayer by the van der Waals force (Pavlík et al., 2012; Yang et al., 2020). Ascending to the middle
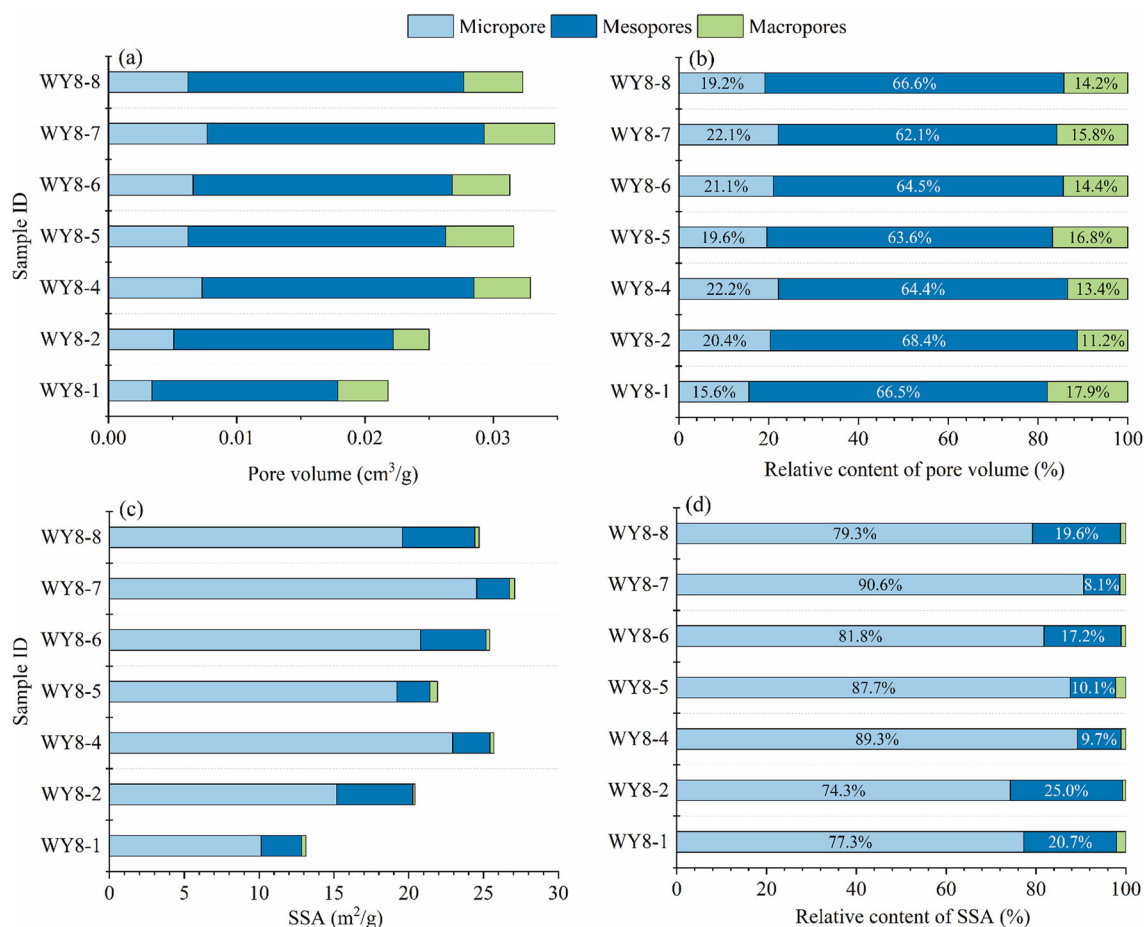
Figure 6. Pore volume, SSA and their percentage distribution for micropore, mesopore, and macropore.
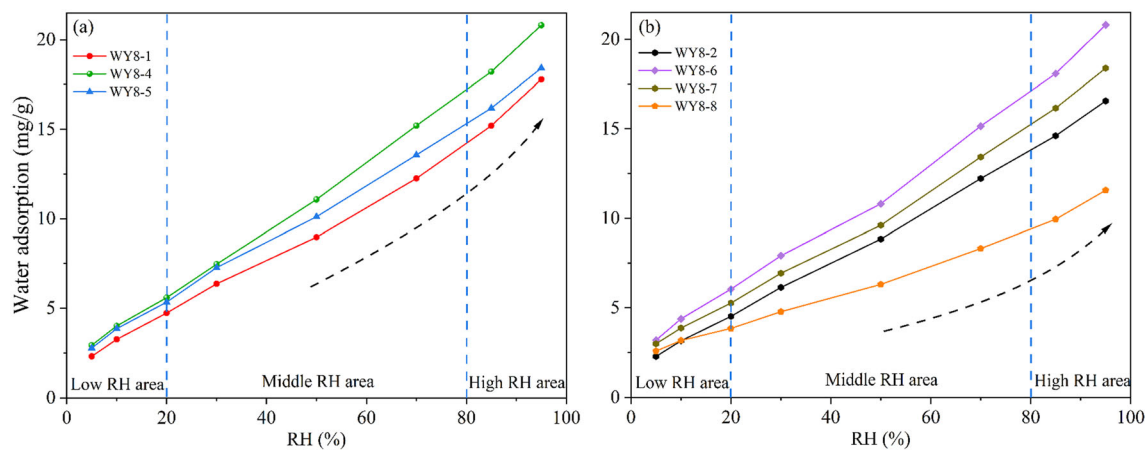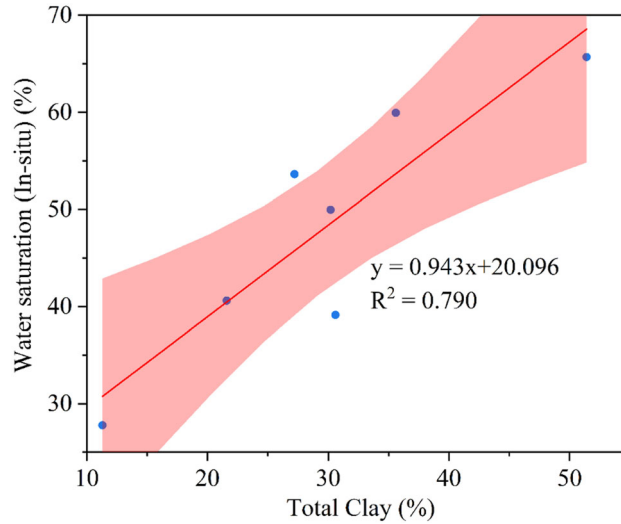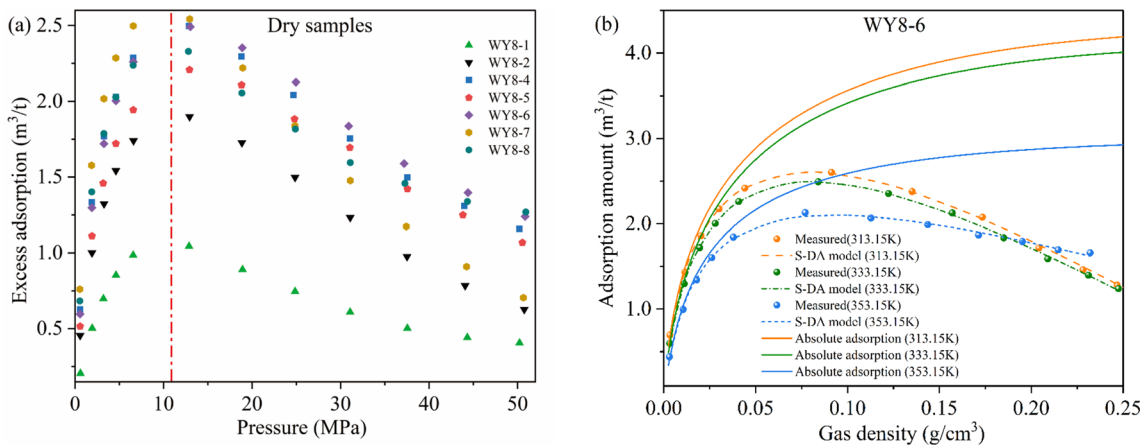

Figure 7. Water vapor adsorption isotherms of the Wufeng–Longmaxi shale.

Figure 8. Correlation between water saturation and total clay content.

Figure 9. (**a**) Measured excess methane–shale adsorption of dry shale samples at 333.15 K. (**b**) Comparison between excess and absolute adsorption isotherms in the dry shale sample WY8-6 at different temperatures.

RH area, the water uptake amount increased gradually, and the multilayer adsorption was mostly determined by H_2O–H_2O interactions due to the interaction between the shale surface and water molecules above the monolayer weakens with increase in distance (i.e., hydrogen bonds) (Feng et al., 2018; Shen et al., 2018). Moreover, with the RH continuing to increase (high RH area), capillary condensation of water molecules caused a rapid and endless increase in water uptake amount (Li et al., 2021a, 2021b).

The actual in situ water saturation collected from the coring site correlated well with the total clay content, with R^2 of 0.79 (Fig. 8, Table 2). The reason for this is that the hydrophilic, charged pores associated with clay make water molecules are more likely to adsorb on the surface due to hydrogen bonding effects (Yang et al., 2020). Additionally, the clay in the Wufeng–Longmaxi shale consists of chlorite, illite, and mixed-layer illite–smectite and does not contain montmorillonite with large interlayer space and water storage capacity. Thus, the
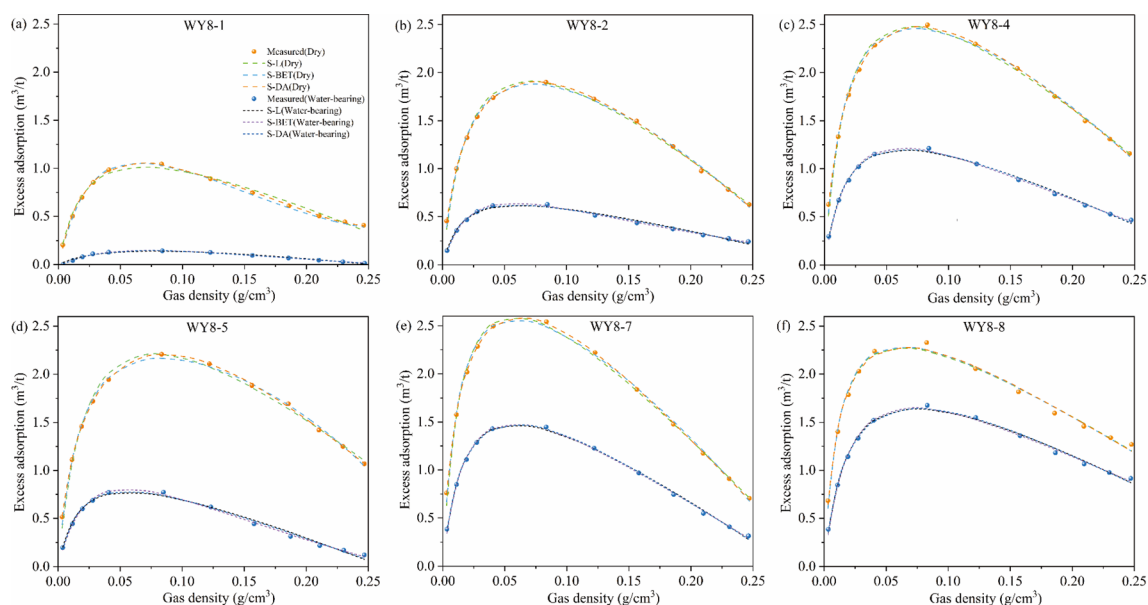
Figure 10. Comparison of excess methane–shale adsorption in dry and water-bearing shale samples, as well as modeling results of various models.

actual in situ water saturation of the Wufeng–Longmaxi shale primarily correlates with clay content, regardless of clay types (Feng et al., 2018; Yang et al., 2020).

Characteristics and Different Modeling Results of Methane–Shale Adsorption Under High Pressure

Characteristics of Methane–Shale Adsorption

The measured excess adsorption isotherms exhibited similar characteristics, with the excess adsorption amount increasing rapidly at low pressures, reaching a maximum at approximately 11 MPa and then, decreasing with pressure increases (Fig. 9a). The Gibbs excess adsorption phenomenon is due to the neglect of the volume occupied by the adsorbate on the surface of the adsorbent, which cannot be precisely measured (Chen et al., 2019; Dang et al., 2020). The methane–shale adsorption isotherms of different samples varied significantly and the amount of methane adsorption amount V_M ranged from 1.521 to 4.079 m³/t.

To facilitate the following modeling study, the excess adsorption isotherms were established by changing the x-axis from pressure to gas density (Figs. 10b and 12). In addition, the temperature had

a negative impact on adsorption amount (Fig. 9b) (Zou et al., 2019; Dang et al., 2020). Moreover, the comparison of excess methane adsorption isotherms on dry samples and samples with water saturation restored is demonstrated in Figure 10. The excess adsorption amount of samples with water saturation restored was lower than in dry samples, and the reduction was ascribed to the occupation of the adsorption site by water molecules and the blockage of pores for gas adsorption by capillary condensation of water molecules (Fig. 18b) (Zou et al., 2019; Yang et al., 2020).

Supercritical Excess Adsorption Isotherms Model and Evaluation

The best-fitting model and its theory contribute to comprehending the mechanism of methane–shale adsorption (Table 4). The S–L, S–BET, and S–DA models were selected to fit the excess measured excess adsorption data to acquire the values of the parameters to be determined in each model using the Levenberg–Marquardt optimization algorithm in Origin software (Table 4). The comparison of the results of the modeling of several models is demonstrated in Figures 9b and 10. It is obvious that all three models exhibited $R^2 > 0.985$ in all cases over the en-

Table 4. Fitting parameters of various models for supercritical excess methane adsorption in dry and water-bearing shale samples

| Sample types	Models	S-L					S-BET						S-DA					
		V_L (m³/t)	P_L (MPa)	ρ_{ads} (g/cm³)	R^2	AIC_C	k_1	k_2	k_3	ρ_{ads} (g/cm³)	R^2	AIC_C	V_M (m³/t)	D	n	ρ_{ads} (g/cm³)	R^2	AIC_C
Dry samples	WY8-1	1.8552	4.5898	0.3103	0.985	−74.979	0.0177	0.3938	1.8454	0.3823	0.988	−74.276	1.5208	0.054	2.443	0.3234	0.990	−90.707
	WY8-2	3.5883	4.9292	0.3058	0.994	−71.666	0.0074	0.3253	−0.3654	0.2938	0.996	−71.680	3.2914	0.149	1.715	0.3042	0.999	−93.697
	WY8-4	4.2332	4.0026	0.3488	0.993	−66.453	0.0051	0.266	−0.2668	0.3278	0.995	−64.906	3.9801	0.104	1.871	0.346	0.999	−87.319
	WY8-5	4.0189	5.0567	0.3533	0.990	−63.777	0.0065	0.3054	−0.5392	0.3115	0.995	−68.485	3.8831	0.163	1.633	0.3444	0.999	−92.652
	WY8-7	4.2847	3.0566	0.2996	0.994	−63.820	0.0038	0.2596	−0.2269	0.2899	0.996	−62.737	4.0581	0.092	1.916	0.2976	0.999	−93.510
	WY8-8	3.3636	2.4228	0.3963	0.988	−63.394	0.0042	0.3026	−0.0095	0.3997	0.989	−59.002	3.1356	0.033	2.447	0.4023	0.990	−60.893
	WY8-6 (40 °C)	4.4587	3.8137	0.3624	0.986	−58.190	0.0048	0.2614	−0.3039	0.3368	0.988	−57.408	4.2708	0.119	1.771	0.3569	0.998	−77.782
	WY8-6 (60 °C)	4.3551	4.3979	0.3592	0.993	−65.612	0.0055	0.2646	−0.3088	0.3317	0.995	−65.528	4.0787	0.115	1.825	0.3556	0.999	−86.895
	WY8-6 (80 °C)	3.2282	4.1105	0.5108	0.997	−80.248	0.0071	0.3143	0.1619	0.6208	0.997	−76.589	2.99	0.044	2.326	0.5242	0.996	−75.172
Water-bearing samples	WY8-1	0.3780	10.526	0.2525	0.963	−104.55	0.2054	1.020	13.5987	0.2693	0.980	−117.177	0.2384	0.077	2.707	0.2619	0.975	−116.312
	WY8-2	1.0229	3.3019	0.3188	0.9813	−87.430	0.0229	0.7656	3.0175	0.3997	0.996	−102.830	0.8662	0.031	2.706	0.3332	0.986	−87.944
	WY8-4	2.0526	3.7518	0.3187	0.993	−83.852	0.0116	0.4526	0.5789	0.3475	0.996	−87.489	1.7861	0.059	2.285	0.327	0.994	−81.809
	WY8-5	1.3842	3.6639	0.2622	0.984	−78.126	0.0188	0.5609	1.6891	0.2771	0.994	−86.755	1.1779	0.062	2.345	0.2659	0.987	−77.553
	WY8-7	2.5847	3.5962	0.2784	0.996	−82.885	0.0084	0.3849	0.1204	0.2832	0.997	−80.719	2.2921	0.081	2.088	0.2808	0.998	−84.062
	WY8-8	2.744	3.9692	0.3756	0.991	−76.135	0.0088	0.361	0.2379	0.4138	0.992	−73.523	2.4571	0.064	2.184	0.3843	0.992	−73.739
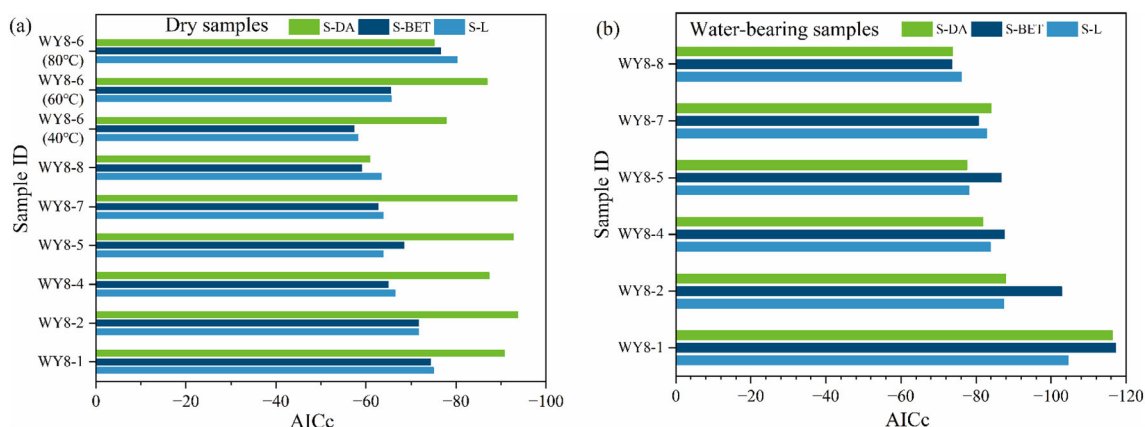
Figure 11. AIC_c value of various models in methane adsorption on dry and water-bearing shale samples.

tire range of gas densities. However, R^2 is invalid for model evaluation, as increasing the number of parameters results in values of R^2 increasing (Spiess & Neumeyer, 2010; Dang et al., 2020).

The AIC_c method was introduced to identify the optimal model due to its use of both goodness-of-fit (accuracy) and variability (precision) to assess the capacity of various models to explain a given dataset (Dang et al., 2020). The optimal model is the one with the lowest AICc value. The AIC_c value can be calculated as follows (Dang et al., 2020):

$$AICc = N\ln\left(\frac{\sum_{i=1}^{N}(V_e - V_m)^2}{N}\right) + 2K + \frac{2K(K+1)}{N-K-1} \tag{15}$$

where N is number of measured points, K is number of fitted parameters, V_e is measured data, and V_m is modeling data.

The AIC_c values of the dry samples and the samples with restored water saturation were calculated by Eq. (15) (Table 4, Fig. 11). For the dry samples, the AIC_c values of each model decreased in order of S–BET > S–L > S–DA, revealing that the supercritical excess adsorption model based on DA was the optimal model (Fig. 11a). The S–BET model was poorly fitted because its theoretical assumptions are inconsistent with the nature of supercritical gases (Tian et al., 2016). The optimal S–DA demonstrates that, in dry shale, the methane molecules first occurred in the micropores as volume filling, followed by monolayer adsorption on the surface of mesopores and macropores (Fig. 18a).

The AIC_c values of the S–DA model in samples with restored water saturation restored were, how-

ever, not the minimum (Fig. 11b). This may be attributed to progressive blockage of micropores caused by capillary condensation of water molecules and the thickening water film from adsorbed water (Yang et al., 2020). On the surface of mesopores, macropores, or water film, the methane molecules are directly adsorbed (Fig. 18b).

Absolute Adsorption Amount

The absolute adsorption isotherm can be derived from the measured excess adsorption data by using the methane density of adsorbed phase and Eq. (9). As shown in Figure 9b, the absolute adsorption amount was always larger than that of excess adsorption and the difference was more significant under high pressure. This finding suggests that the measured excess adsorption amount should be corrected to the absolute adsorption amount, otherwise the content of adsorbed gas will be seriously underestimated (Zhou et al., 2018; Dang et al., 2020).

DISCUSSION

Effect of Shale Composition on Pore Structure

As analyzed above, shale pores are developed in OM and formed between inorganic mineral grains. The pore structure is naturally related to the composition of the shale. The storage space for the accumulation of shale gas is comprised of pores associated with OM, and the TOC content had a
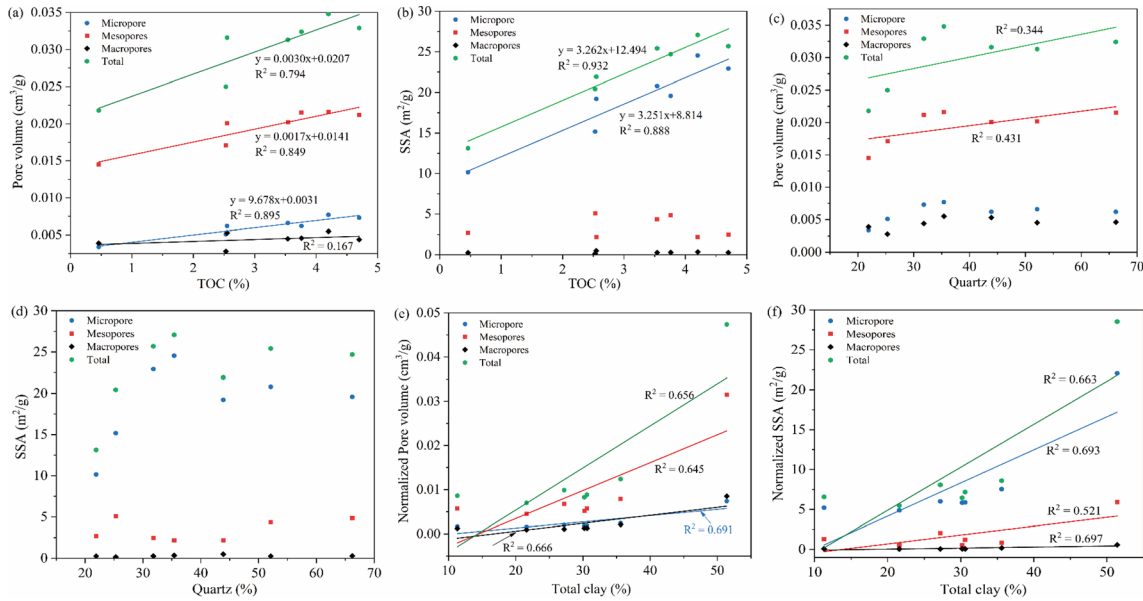
Figure 12. Correlations of the composition of the shale with pore volume and SSA of the Wufeng–Longmaxi shale in the Weiyuan area.

strong correlation with pore volume (Fig. 12a). In addition, TOC content exhibited a significant positive correlation with both micropore and total SSA, with R^2 of 0.888 and 0.932 (Fig. 12b). The relationships suggest that an abundance of OM facilitated improving the pore volume and SSA while mainly controlling the development of micropores.

There was only a weakly positive relationship between quartz and mesopore and total pore volume, with R^2 of 0.431 and 0.344 (Fig. 12c and d). The reason for this is that an abundance of hard framework pores was formed during the opal transformed into quartz microcrystals (Guo et al., 2020). The pore volume and SSA were normalized to the per unit TOC content (1%) to avoid high TOC content obscuring the importance of clay minerals to the shale pores. Then, the clay content exhibited a positive correlation with both pore volume and SSA (Fig. 12e and f), suggesting that clay minerals did contribute to the formation of shale pores (Pan et al., 2015; Zhang et al., 2018).

Effect of Shale Composition on Methane–Shale Adsorption Capacity

The methane–shale adsorption capacity is significantly determined by shale composition (Chal-

mers & Bustin, 2008; Guo et al., 2020). Strong positive correlations existed between TOC content and the methane–shale adsorption capacity, with R^2 of 0.945, demonstrating that the shale adsorption capacity increased with TOC content (Fig. 13a). The reason for this is that sufficient OM is conducive to the growth of abundant organic pores with larger SSA, which further offers methane molecules adsorption sites. Moreover, polar functional groups in OM are more attractive for the adsorption of methane than hydrophilic inorganic matter, and approximately 46.5–81.5% of the adsorption capacity can be attributed to OM (Zhang et al., 2012; Yang et al., 2015).

Quartz and clay minerals predominate in the Wufeng–Longmaxi shale. The methane–shale adsorption capacity correlated well with quartz, with R^2 of 0.603 (Fig. 13b), due to hard framework pores associated with quartz microcrystals facilitated OM enrichment and the formation of organic pores (Guo et al., 2020).

The adsorption capacity was normalized to the per unit TOC content (1%) to avoid high TOC content obscuring the importance of clay minerals to adsorption capacity. Then, the clay content exhibited an obvious positive correlation with adsorption capacity, with R^2 of 0.776 (Fig. 13c), suggesting that clay minerals also improved the methane–shale
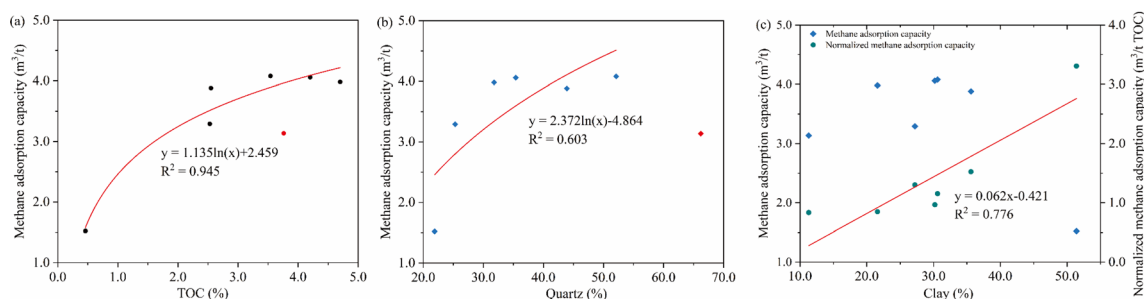
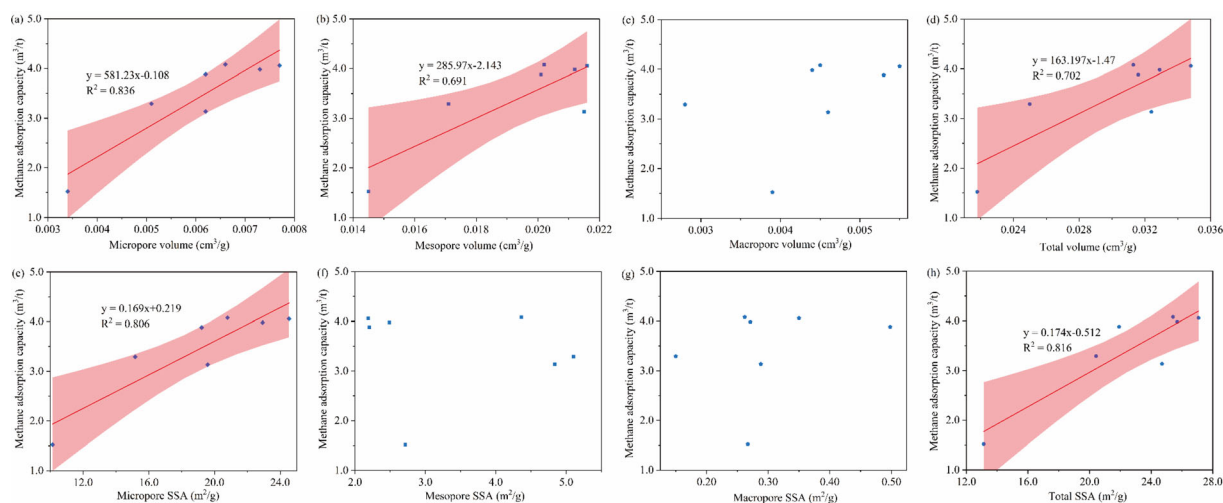**Figure 13.** Correlation between adsorption capacity and shale composition.

Figure 14. Correlation between the methane adsorption capacity and the pore structure.

adsorption capacity due to their larger negatively charged SSA (Zhu et al., 2020). Previous studies reported that approximately 45–60% of methane–shale adsorption capacity was provided by clay minerals (Rexer et al., 2014).

### Effect of Pore Structure on Methane–Shale Adsorption Capacity

Shale adsorption capacity is closely correlated with pore structure, especially micropores volume and SSA (Yang et al., 2016a, 2016b; Wang et al., 2021). The adsorption capacity had a strong positive relationship with both micropore volume and SSA, with R^2 of 0.836 and 0.806, respectively (Fig. 14), and the amount was determined by the pore SSA. In addition, the relationships between pore structure,

adsorption capacity and TOC content illustrated in Figures 12 and 13 revealed the importance of abundant micropores associated with OM in adsorption capacity.

Effect of Temperature on Methane–Shale Adsorption Capacity

The maximum methane adsorption amount was significantly negatively correlated with temperature, with R^2 that all exceeded 0.85 (Fig. 15). As the temperature increased from 40 to 80 °C, the methane adsorption capacity decreased from 4.27 to 2.99 m³/t, a 30% decrease.

Thermodynamic parameters are introduced to supply important information about the adsorption process. Six adsorption capacities, ranging from 0.5
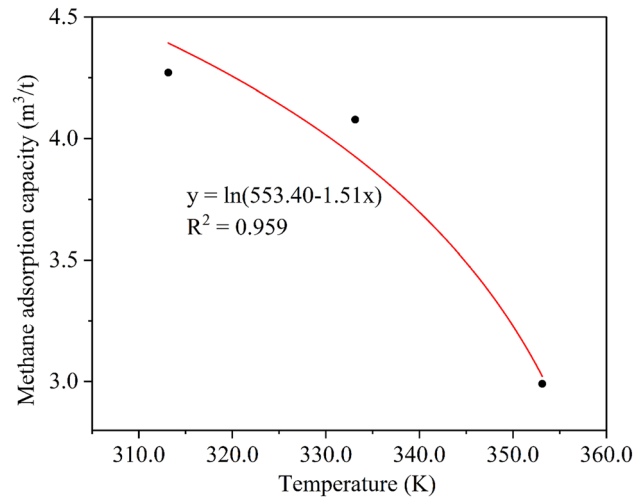
Figure 15. Correlation between temperature and adsorption capacity.
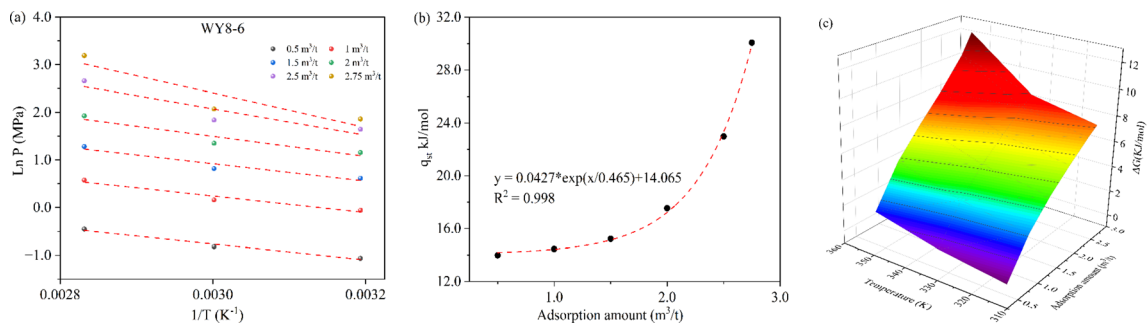
Figure 16. (**a**) Plot of ln P vs. 1/T for various absolute adsorption amounts. (**b**) Relationship between q_{st} and adsorption amount. (**c**) Fluctuation of ΔG with methane adsorption amount at different temperatures.

to 2.75 cm^3/g for sample WY8-6, were selected, and the DA model can be used to calculate the gas pressure P of each adsorption capacity at different temperatures (Figs. 9b, 16a). The q_{st}, ΔH, and ΔS are listed in Table 5. The q_{st} of sample WY8-6 varied between 13.99 and 30.07 kJ/mol, indicating that methane–shale adsorption belongs to the physisorption because q_{st} was lower than 41 kJ/mol (Dang et al., 2020). The ΔH varied between $-$ 13.99 and $-$ 30.07 kJ/mol, negative values, suggesting that methane adsorption was an exothermic process. The negative sign of ΔS suggests that the disorder of methane molecules on the surface of shale pores descended during the adsorption process due to methane molecules transforming from a three-di-

mensional motion state to a two-dimensional adsorption state.

As illustrated in Figure 16b, the q_{st} was significantly positively correlated with adsorption amount. As the amount of adsorption increased, more methane molecules existed in the pores and the methane–methane intermolecular interaction became significant, resulting in an increase in isosteric adsorption heat.

Figure 16c depicts the variation of ΔG with methane adsorption amount at different temperatures. The negative value of ΔG at low temperature indicates that the methane–shale adsorption was thermodynamically spontaneous. However, as the temperature increased, the positive value of ΔG

Table 5. Thermodynamic characteristics of methane adsorption in shale

Absolute adsorption amount (m³/t)	Fitting equations	Adjusted R^2	q_{st} (kJ/mol)	ΔH (kJ/mol)	ΔS (J/mol · K)	ΔG (kJ/mol) Temperature		
						313.15 K	333.15 K	353.15 K
0.5	y = − 1682.29x + 4.28	0.954	13.99	− 13.99	− 44.14	− 0.167	0.715	1.598
1.0	y = − 1737.56x + 5.46	0.911	14.45	− 14.45	− 53.99	2.456	3.216	4.629
1.5	y = − 1831.73x + 6.42	0.873	15.22	− 15.22	− 62.03	4.205	5.040	6.705
2.0	y = − 2110.14x + 7.83	0.813	17.54	− 17.54	− 74.02	5.616	6.518	8.599
2.5	y = − 2764.35x + 10.37	0.731	22.98	− 22.98	− 95.39	6.891	7.872	10.747
2.75	y = − 3617.04x + 13.26	0.703	30.07	− 30.07	− 119.82	7.453	8.516	12.304

Table 6. Comparison of the adsorption capacity of dry and water-bearing shale

Sample ID	Methane adsorption capacity			
	V_M(Dry) (m³/t)	V_M(Water-bearing) (m³/t)	Absolute difference[a] (m³/t)	Relative difference[b] (%)
WY8-1	1.5208	0.2384	1.2824	84.32
WY8-2	3.2914	0.8662	2.4252	73.68
WY8-4	3.9801	1.7861	2.194	55.12
WY8-5	3.8831	1.1779	2.7052	69.67
WY8-7	4.0581	2.2921	1.766	43.52
WY8-8	3.1356	2.4571	0.6785	21.64

[a]Absolute difference (AD) = V_M(Dry)- V_M(Water-bearing)
[b]Relative difference (RD) = (V_M(Dry)- V_M(Water-bearing))/ V_M(Dry)*100%

indicated that the reverse adsorption reaction of methane on shale occurred spontaneously, and methane molecules were more easily desorbed from shale, which is consistent with the fact that the process of methane adsorption is exothermic. Moreover, the values of ΔG increased with temperature and adsorption amount, indicating that the process of methane–shale adsorption became more difficult at higher temperatures (Dang et al., 2020).
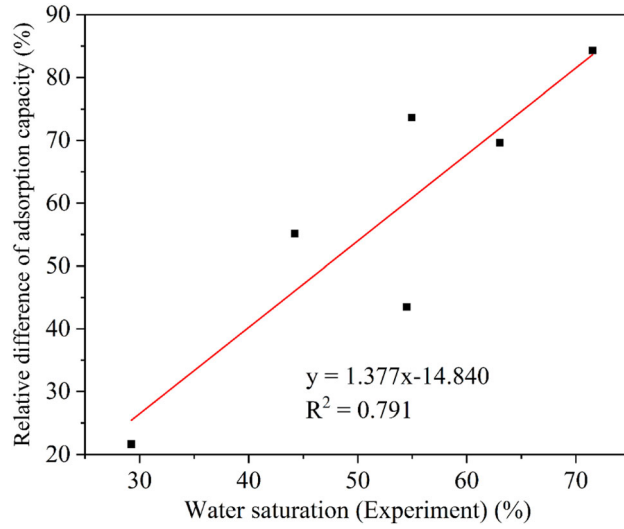
Effect of Water Saturation on Methane–Shale Adsorption Capacity

Shale adsorption capacity can be largely reduced compared to dry shale, and the adsorption capacity at equilibrium moisture was 58.3% and 71.5% of that in the dry state, respectively (Hao et al., 2013). In this work, the relative difference in adsorption capacity of dry and water-bearing shale increased with water saturation (experimental), with the adsorption capacity of water-bearing shales decreasing by 21–84% at water saturation of 30–71% compared to that of dry shales (Table 6, Fig. 17).

As illustrated in Figure 18a, as for dry shale, the methane molecules first occurred in the micropores as volume filling, followed by monolayer adsorption on non-micropores based on the theory of micropore volume filling and analysis of thermodynamic parameters (Dubinin & Astakhov, 1971; Dang et al., 2020). Methane molecules were adsorbed on the surface of hydrophobic (OM) and hydrophilic (inorganic minerals) sites as adsorbed gas due to van der Waals forces between the gas molecules and the solid surface, and the rest existed in the pore space as free gas.

As illustrated in Figure 18b, with the water saturation increasing, the water molecules were preferentially adsorbed on the surface of hydrophilic pore wall due to the strong hydrogen bond. Next, the abundance of pores for gas adsorption was progressively blocked by clusters of water and capillary condensation of water molecules. Additionally, the

Figure 17. Correlation between water saturation (experimental) and the relative difference in adsorption capacity of dry and water-bearing shale.
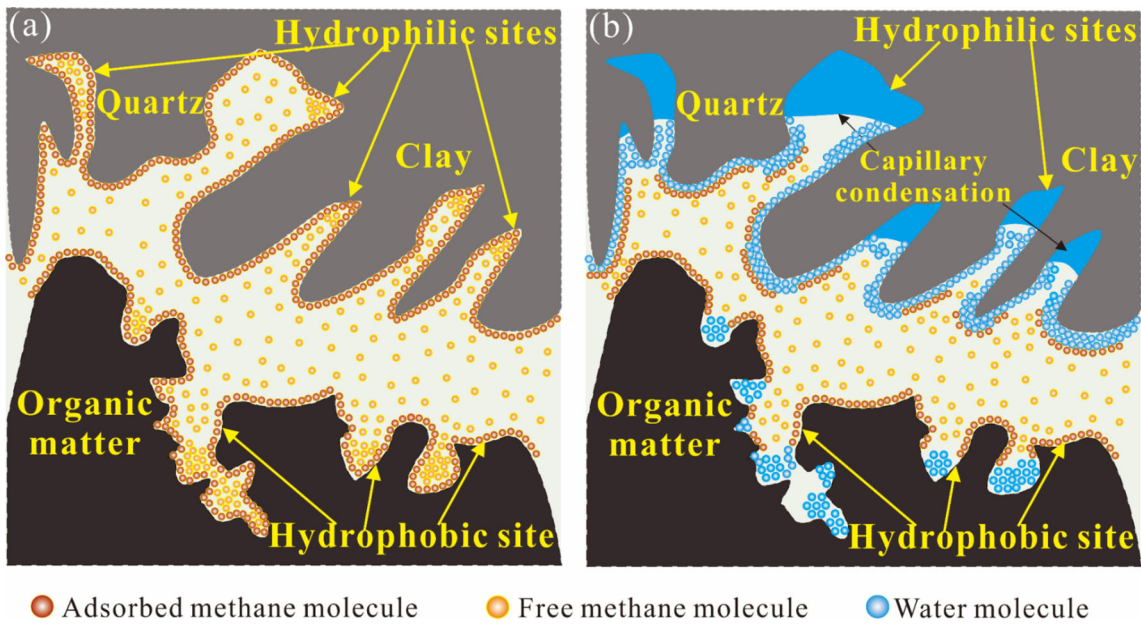
Figure 18. Schematic of the methane–shale adsorption mechanism in dry and water-bearing shale.

solid–gas interaction transformed into the liquid–gas interaction due to the formation of an adsorbed water film; the methane molecules were adsorbed on the water film, reducing the adsorption capacity (Shen et al., 2018; Yang et al., 2020).

CONCLUSIONS

In this study, the characteristics of methane–shale adsorption were investigated under a wide range of pressures and water saturation, and the supercritical excess adsorption models were evalu-

ated by the AIC$_c$ method. The effects of shale composition, pore structure, temperature, and water saturation on the adsorption capacity were discussed deeply, and the occurrence mechanism of shale gas in dry shale and water-bearing shale was elaborated in detail. Four detailed conclusions can be drawn.

(1) Methane–shale adsorption exhibits the Gibbs excess adsorption phenomenon under high pressure due to the neglect of the volume occupied by adsorbate on the adsorbent's surface. The excess adsorption amount needs be corrected to absolute adsorption amount, otherwise it will be seriously underestimated. The DA-based supercritical methane excess adsorption (S–DA) model is the optimal model determined by the AICc method, demonstrating that in dry shale, methane molecules first occurred in micropores as volume filling, followed by monolayer adsorption on the surface of non-micropores.

(2) The methane adsorption amount V_M ranged from 1.521 to 4.079 m^3/t. In terms of methane–shale adsorption capacity, the TOC content is the key factor due to both the pore volume and the SSA being contributed mainly by abundant micropores associated with OM. Clay minerals also improved the adsorption capacity due to their larger negatively charged SSA.

(3) Thermodynamic parameters reveal that the adsorption of methane on shale is an exothermic process. The process of methane–shale adsorption became more difficult at higher temperatures. As the temperature increased from 40 to 80 °C, the methane adsorption capacity decreased from 4.27 to 2.99 m^3/t, a 30% decrease.

(4) The actual in situ water saturation correlated primarily with clay content, regardless of clay types, and increased with clay content. The formation of adsorbed water film and the blockage of pores for gas adsorption by clusters of water molecules and capillary condensation significantly lowered the adsorption capacity. The relative difference in adsorption capacity increased with water saturation (experimental), with the adsorption capacity of water-bearing shales decreasing by 21–84% at a water saturation of 30–71% compared to dry shales.

DECLARATIONS

Conflict of Interest The authors declare that there are no conflicts of interest regarding the publication of this paper.

REFERENCES

Borjigin, T., Shen, B., Yu, L., Yang, Y., Zhang, W., Tao, C., Xi, B., Zhang, Q., Bao, F., & Qin, J. (2017). Mechanisms of shale gas generation and accumulation in the Ordovician Wufeng-Longmaxi Formation, Sichuan Basin SW China. *Petroleum Exploration and Development, 44*(1), 69–78.

Brunauer, S., Emmett, P. H., & Teller, E. (1938). Adsorption of gases in multimolecular layers. *Journal of the American Chemical Society, 60*, 309–319.

Chalmers, G. R. L., & Bustin, R. M. (2008). Lower Cretaceous gas shales in northeastern British Columbia, Part I: Geological controls on methane sorption capacity. *Bulletin of Canadian Petroleum Geology, 56*(1), 1–21.

Chen, L., Zuo, L., Jiang, Z., Jiang, S., Liu, K., Tan, J., & Zhang, L. (2019). Mechanisms of shale gas adsorption: Evidence from thermodynamics and kinetics study of methane adsorption on shale. *Chemical Engineering Journal, 361*, 559–570.

Chen, M., Kang, Y., Zhang, T., Li, X., Wu, K., & Chen, Z. (2018). Methane adsorption behavior on shale matrix at in-situ pressure and temperature conditions: Measurement and modeling. *Fuel, 228*, 39–49.

Curtis, J. B. (2002). Fractured shale-gas systems. *AAPG Bulletin, 86*(11), 1921–1938.

Dang, W., Zhang, J., Nie, H., Wang, F., Tang, X., Wu, N., Chen, Q., Wei, X., & Wang, R. (2020). Isotherms, thermodynamics and kinetics of methane-shale adsorption pair under supercritical condition: Implications for understanding the nature of shale gas adsorption process. *Chemical Engineering Journal, 383*, 123191.

Dubinin, M. M., & Astakhov, V. A. A. (1971). Development of the concept of volume filling of micropores in the adsorption of gases and vapors by microporous adsorbents. *Bulletin of the Academy of Sciences of the Ussr Division of Chemical Science, 20*(1), 13–16.

Fan, C., Li, H., Qin, Q., He, S., & Zhong, C. (2020). Geological conditions and exploration potential of shale gas reservoir in Wufeng and Longmaxi Formation of southeastern Sichuan Basin, China. *Journal of Petroleum Science and Engineering, 191*, 107138.

Feng, D., Li, X., Wang, X., Li, J., Sun, F., Sun, Z., Zhang, T., Li, P., Chen, Y., & Zhang, X. (2018). Water adsorption and its impact on the pore structure characteristics of shale clay. *Applied Clay Science, 155*, 126–138.

Gasparik, M., Bertier, P., Gensterblum, Y., Ghanizadeh, A., Krooss, B. M., & Littke, R. (2014). Geological controls on the

methane storage capacity in organic-rich shales. *International Journal of Coal Geology, 123*, 34–51.

Gibbs, J. W. (1878). On the equilibrium of heterogeneous substances. *American Journal of Science*. https://doi.org/10.2475/ajs.s3-16.96.441.

Gou, Q., Xu, S., Hao, F., Yang, F., Shu, Z., & Liu, R. (2021). The effect of tectonic deformation and preservation condition on the shale pore structure using adsorption-based textural quantification and 3D image observation. *Energy, 219*, 119579.

Gou, Q., Xu, S., Hao, F., Zhang, B., Shu, Z., Yang, F., Wang, Y., & Li, Q. (2020). Quantitative calculated shale gas contents with different lithofacies: A case study of Fuling gas shale, Sichuan Basin, China. *Journal of Natural Gas Science and Engineering, 76*, 103222.

Guan, Q., Dong, D., Wang, S., Huang, J., Wang, Y., Lu, H., & Zhang, C. (2016). Preliminary study on shale gas microreservoir characteristics of the Lower Silurian Longmaxi Formation in the southern Sichuan Basin, China. *Journal of Natural Gas Science and Engineering, 31*, 382–395.

Guo, X., Li, Y., Borjigen, T., Wang, Q., Yuan, T., Shen, B., Ma, Z., & Wei, F. (2020). Hydrocarbon generation and storage mechanisms of deep-water shelf shales of Ordovician Wufeng Formation-Silurian Longmaxi Formation in Sichuan Basin, China. *Petroleum Exploration and Development, 47*(1), 204–213.

Han, L., Li, X., Guo, W., Ju, W., Cui, Y., Liu, Z., Qian, C., & Shen, W. (2022). Characteristics and dominant factors for natural fractures in deep shale gas reservoirs: A case study of the Wufeng-Longmaxi Formations in Luzhou Block Southern, China. *Lithosphere, 2022*(1), 9662175.

Hao, F., Zou, H., & Lu, Y. (2013). Mechanisms of shale gas storage: Implications for shale gas exploration in China. *AAPG Bulletin, 97*(8), 1325–1346.

Hughes, J. D. (2013). A reality check on the shale revolution. *Nature, 494*(7437), 307–308.

Ji, L., Zhang, T., Milliken, K. L., Qu, J., & Zhang, X. (2012). Experimental investigation of main controls to methane adsorption in clay-rich rocks. *Applied Geochemistry, 27*(12), 2533–2545.

Jia, C., Zheng, M., & Zhang, Y. (2012). Unconventional hydrocarbon resources in China and the prospect of exploration and development. *Petroleum Exploration and Development, 39*(2), 139–146.

Langmuir, I. (1918). The adsorption of gases on plane surfaces of glass, mica and platinum. *Journal of the American Chemical Society, 40*(9), 1361–1403.

Li, J., Li, B., & Gao, Z. (2021a). Water vapor adsorption behavior in shale under different temperatures and pore structures. *Natural Resources Research, 30*(3), 2789–2805.

Li, Q., Li, B., Mei, W., & Liu, Y. (2022). Genesis and sources of natural gas in fold-and-thrust belt: The Middle Permian in the NW Sichuan Basin. *Marine and Petroleum Geology, 140*, 105638.

Li, X., Jiang, Z., Jiang, S., Wang, S., & Cao, X. (2021b). Synergetic effects of matrix components and diagenetic processes on pore properties in the Lower Cambrian shale in Sichuan Basin, South China. *Journal of Natural Gas Science and Engineering, 94*(4–5), 104072.

Loucks, R. G., Reed, R. M., Ruppel, S. C., & Hammes, U. (2012). Spectrum of pore types and networks in mudrocks and a descriptive classification for matrix-related mudrock pores. *AAPG Bulletin, 96*(6), 1071–1098.

Loucks, R. G., Reed, R. M., Ruppel, S. C., & Jarvie, D. M. (2009). Morphology, genesis, and distribution of nanometer-scale pores in siliceous mudstones of the Mississippian Barnett shale. *Journal of Sedimentary Research, 79*(12), 848–861.

Ma, X., Li, X., Liang, F., Wan, Y., Shi, Q., Wang, Y., Zhang, X., Che, M., Guo, W., & Guo, W. (2020). Dominating factors on

well productivity and development strategies optimization in Weiyuan shale gas play, Sichuan Basin. *SW China. Petroleum Exploration and Development, 47*(3), 594–602.

Middleton, R. S., Gupta, R., Hyman, J. D., & Viswanathan, H. S. (2017). The shale gas revolution: Barriers, sustainability, and emerging opportunities. *Applied Energy, 199*, 88–95.

Nie, H., Li, P., Dang, W., Ding, J., Sun, C., Liu, M., Wang, J., Du, W., Zhang, P., Li, D., & Su, H. (2022). Enrichment characteristics and exploration directions of deep shale gas of Ordovician-Silurian in the Sichuan Basin and its surrounding areas, China. *Petroleum Exploration and Development, 49*(4), 744–757.

Pan, L., Xiao, X., Tian, H., Zhou, Q., Chen, J., Li, T., & Wei, Q. (2015). A preliminary study on the characterization and controlling factors of porosity and pore structure of the Permian shales in Lower Yangtze region, Eastern China. *International Journal of Coal Geology, 146*, 68–78.

Pavlík, Z., Žumár, J., Medved, I., & Černý, R. (2012). Water vapor adsorption in porous building materials: Experimental measurement and theoretical analysis. *Transport in Porous Media, 91*(3), 939–954.

Peng, N. (2019). Organic nanopore structure and fractal characteristics of Wufeng and lower member of Longmaxi shales in southeastern Sichuan, China. *Marine and Petroleum Geology, 103*, 456–472.

Qian, C., Li, X., Shen, W., Zhang, Q., Guo, W., Hu, Y., Cui, Y., & Jia, Y. (2022). Study on the pore structure and fractal characteristics of different lithofacies of wufeng–longmaxi formation shale in Southern Sichuan Basin, China. *ACS Omega, 7*, 8724–8738.

Qiu, Z., Liu, B., Dong, D., Lu, B., Yawar, Z., Chen, Z., & Schieber, J. (2020). Silica diagenesis in the Lower Paleozoic Wufeng and Longmaxi Formations in the Sichuan Basin, South China: Implications for reservoir properties and paleooproductivity. *Marine and Petroleum Geology, 121*, 104594.

Rexer, T. F. T., Benham, M. J., Aplin, A. C., & Thomas, K. M. (2013). Methane adsorption on shale under simulated geological temperature and pressure conditions. *Energy & Fuels, 27*(6), 3099–3109.

Rexer, T. F., Mathia, E. J., Aplin, A. C., & Thomas, K. M. (2014). High-pressure methane adsorption and characterization of pores in posidonia shales and isolated kerogens. *Energy & Fuels, 28*(5), 2886–2901.

Ross, D. J. K., & Bustin, R. M. (2008). Characterizing the shale gas resource potential of Devonian-Mississippian strata in the Western Canada sedimentary basin: Application of an integrated formation evaluation. *AAPG Bulletin, 92*(1), 87–125.

Sakurovs, R., Day, S., Weir, S., & Duffy, G. (2007). Application of a modified Dubinin-Radushkevich equation to adsorption of gases by coals under supercritical conditions. *Energy & Fuels, 21*(2), 992–997.

Shen, W., Li, X., Lu, X., Guo, W., Zhou, S., & Wan, Y. (2018). Experimental study and isotherm models of water vapor adsorption in shale rocks. *Journal of Natural Gas Science and Engineering, 52*, 484–491.

Shen, W., Li, X., Ma, T., Cai, J., Lu, X., & Zhou, S. (2021). High-pressure methane adsorption behavior on deep shales: Experiments and modeling. *Physics of Fluids, 33*(6), 063103.

Sing, K. S. W. (1985). Reporting physisorption data for gas/solid systems with special reference to the determination of surface area and porosity (Recommendations 1984). *Pure and Applied Chemistry, 57*(4), 603–619.

Spiess, A. N., & Neumeyer, N. (2010). An evaluation of R2 as an inadequate measure for nonlinear models in pharmacological and biochemical research: A Monte Carlo approach. *Bmc Pharmacology, 10*(1), 1–11.

Stueck, H., Houseknecht, D., Franke, D., Gautier, D., Bahr, A., & Ladage, S. (2016). Shale-gas assessment: Comparison of gas-

in-place versus performance-based approaches. *Natural Resources Research, 25*(3), 315–329.

Teng, J., Liu, B., Mastalerz, M., & Schieber, J. (2022). Origin of organic matter and organic pores in the overmature Ordovician-Silurian Wufeng-Longmaxi Shale of the Sichuan Basin, China. *International Journal of Coal Geology, 253*, 103970.

Tian, H., Li, T., Zhang, T., & Xiao, X. (2016). Characterization of methane adsorption on overmature Lower Silurian-Upper Ordovician shales in Sichuan Basin, southwest China: Experimental results and geological implications. *International Journal of Coal Geology, 156*, 36–49.

Wang, L., & Yu, Q. (2016). The effect of moisture on the methane adsorption capacity of shales: A study case in the eastern Qaidam Basin in China. *Journal of Hydrology, 542*, 487–505.

Wang, Y., Liu, L., & Cheng, H. (2021). Gas adsorption characterization of pore structure of organic-rich shale: Insights into contribution of organic matter to shale pore network. *Natural Resources Research, 30*(3), 2377–2395.

Wang, Y., Zhu, Y., Liu, S., & Zhang, R. (2016). Methane adsorption measurements and modeling for organic-rich marine shale samples. *Fuel, 172*, 301–309.

Wei, M., Zhang, L., Xiong, Y., Li, J., & Peng, P. (2016). Nanopore structure characterization for organic-rich shale using the non-local-density functional theory by a combination of N2 and CO2 adsorption. *Microporous and Mesoporous Materials, 227*, 88–94.

Xinhua, M. A., Yang, Y., Wen, L., & Luo, B. (2019). Distribution and exploration direction of medium-and large-sized marine carbonate gas fields in Sichuan Basin, SW China. *Petroleum Exploration and Development, 46*(1), 1–15.

Xu, S., Gou, Q., Hao, F., Zhang, B., Shu, Z., Lu, Y., & Wang, Y. (2020). Shale pore structure characteristics of the high and low productivity wells, Jiaoshiba shale gas field, Sichuan Basin, China: Dominated by lithofacies or preservation condition? *Marine and Petroleum Geology, 114*, 104211.

Xu, S., Hu, E., Li, X., & Xu, Y. (2021). Quantitative analysis of pore structure and its impact on methane adsorption capacity of coal. *Natural Resources Research, 30*(1), 605–620.

Yang, F., Ning, Z., & Liu, H. (2014). Fractal characteristics of shales from a shale gas reservoir in the Sichuan Basin, China. *Fuel, 115*(2014), 378–384.

Yang, F., Ning, Z., Wang, Q., Zhang, R., & Krooss, B. M. (2016a). Pore structure characteristics of lower Silurian shales in the southern Sichuan Basin, China: Insights to pore development and gas storage mechanism. *International Journal of Coal Geology, 156*, 12–24.

Yang, F., Ning, Z., Zhang, R., Zhao, H., & Krooss, B. M. (2015). Investigations on the methane sorption capacity of marine shales from Sichuan Basin, China. *International Journal of Coal Geology, 146*, 104–117.

Yang, R., He, S., Yi, J., & Hu, Q. (2016b). Nano-scale pore structure and fractal dimension of organic-rich Wufeng-Longmaxi shale from Jiaoshiba area, Sichuan Basin: Investigations using FE-SEM, gas adsorption and helium pycnometry. *Marine and Petroleum Geology, 70*, 27–45.

Yang, R., Jia, A., He, S., Hu, Q., Dong, T., Hou, Y., & Yan, J. (2020). Water adsorption characteristics of organic-rich Wufeng and Longmaxi Shales, Sichuan Basin (China). *Journal of Petroleum Science and Engineering, 193*, 107387.

Zhang, J., Li, X., Xie, Z., Li, J., Zhang, X., Sun, K., & Wang, F. (2018). Characterization of microscopic pore types and structures in marine shale: Examples from the Upper Permian Dalong formation, Northern Sichuan Basin, South China. *Journal of Natural Gas Science and Engineering, 59*, 326–342.

Zhang, J., Tang, Y., He, D., Sun, P., & Zou, X. (2020a). Full-scale nanopore system and fractal characteristics of clay-rich lacustrine shale combining FE-SEM, nano-CT, gas adsorption and mercury intrusion porosimetry. *Applied Clay Science, 196*, 105758.

Zhang, L., Xiao, D., Lu, S., Jiang, S., Chen, L., Guo, T., & Wu, L. (2020b). Pore development of the Lower Longmaxi shale in the southeastern Sichuan Basin and its adjacent areas: Insights from lithofacies identification and organic matter. *Marine and Petroleum Geology, 122*, 104662.

Zhang, T., Ellis, G. S., Ruppel, S. C., Milliken, K., & Yang, R. (2012). Effect of organic-matter type and thermal maturity on methane adsorption in shale-gas systems. *Organic Geochemistry, 47*, 120–131.

Zhou, S., Xue, H., Ning, Y., Guo, W., & Zhang, Q. (2018). Experimental study of supercritical methane adsorption in Longmaxi shale: Insights into the density of adsorbed methane. *Fuel, 211*, 140–148.

Zhu, H., Ju, Y., Huang, C., Chen, F., Chen, B., & Yu, K. (2020). Microcosmic gas adsorption mechanism on clay-organic nanocomposites in a marine shale. *Energy, 197*, 117256.

Zou, C., Dong, D., Wang, S., Li, J., Li, X., Wang, Y., Li, D., & Cheng, K. (2010). Geological characteristics and resource potential of shale gas in China. *Petroleum Exploration and Development, 37*(6), 641–653.

Zou, J., Rezaee, R., Xie, Q., & You, L. (2019). Characterization of the combined effect of high temperature and moisture on methane adsorption in shale gas reservoirs. *Journal of Petroleum Science and Engineering, 182*, 106353.